LIMNOLOGY and OCEANOGRAPHY

ASLO

Limnol. Oceanogr. 65, 2020, 1688–1705

doi: 10.1002/lno.11412

The role of water masses in shaping the distribution of redox active compounds in the Eastern Tropical North Pacific oxygen deficient zone and influencing low oxygen concentrations in the eastern Pacific Ocean

Natalya Evans,[1] **Elisabeth Boles**,[2,a] **Jarek V. Kwiecinski**,[2] **Susan Mullen**,[2,b] **Martin Wolf**,[2] **Allan H. Devol**,[3] **Rintaro Moriyasu**,[1] **SungHyun Nam**,[4] **Andrew R. Babbin**,[2] **James W. Moffett**[1*]

[1]Department of Biological Sciences, University of Southern California, Los Angeles, California
[2]Department of Earth, Atmospheric and Planetary Sciences, Massachusetts Institute of Technology, Cambridge, Massachusetts
[3]School of Oceanography, University of Washington, Seattle, Washington
[4]School of Earth and Environmental Sciences/Research Institute of Oceanography, Seoul National University, Seoul, Republic of Korea

Abstract

Oceanic oxygen deficient zones (ODZs) influence global biogeochemical cycles in a variety of ways, most notably by acting as a sink for fixed nitrogen (Codispoti et al. 2001). Optimum multiparameter analysis of data from two cruises in the Eastern Tropical North Pacific (ETNP) was implemented to develop a water mass analysis for the large ODZ in this region. This analysis reveals that the most pronounced oxygen deficient conditions are within the 13°C water (13CW) mass, which is distributed via subsurface mesoscale features such as eddies branching from the California Undercurrent. Nitrite accumulates within these eddies and slightly below the core of the 13CW. This water mass analysis also reveals that the 13CW and deeper Northern Equatorial Pacific Intermediate Water (NEPIW) act as the two Pacific Equatorial source waters to the California Current System. The Equatorial Subsurface Water and Subtropical Subsurface Water are synonymous with the 13CW and this study refers to this water mass as the 13CW based on its history. Since the 13CW has been found to dominate the most pronounced oxygen deficient conditions within the Eastern Tropical South Pacific ODZ and the Peru-Chile Undercurrent, the 13CW and the NEPIW define boundaries for oxygen minimum conditions across the entire eastern Pacific Ocean.

The Pacific Ocean contains two of the largest oxygen deficient zones (ODZs), horizontally extensive regions of water where dissolved oxygen concentrations are low to negligible and respiration is dominated by denitrification (Thamdrup et al. 2012; Breitburg et al. 2018). This volume of low oxygen water originates from reduced ventilation and elevated respiration of sinking organic matter (Gilly et al. 2013), and forms through natural processes (Helly and Levin 2004; Breitburg et al. 2018) as compared to eutrophication driving coastal deoxygenation (Diaz and Rosenberg 2008). These regions have expanded in tropical and subtropical regions over recent decades and it has been proposed that they will expand in the future (Stramma et al. 2010; Schmidtko et al. 2017). A counter argument claims that a potential deepening of the tropical thermocline will

*Correspondence: jmoffett@usc.edu

Additional Supporting Information may be found in the online version of this article.

[a]Present address: Department of Civil and Environmental Engineering, Stanford University, Palo Alto, California
[b]Present address: Department of Earth and Planetary Science, University of California Berkeley, Berkeley, California

Author Contribution Statement: N.E. performed the optimum multiparameter analysis with publicly available tools modified for this publication, measured iodide on the R/V *Falkor*, wrote this manuscript, and coordinated its distribution between authors. E.B., J.V.K., S.M., and M.W. shared equal roles in measuring nitrite and phosphate on the R/V *Falkor*. R.M. optimized the iodine measurements and measured iodate and iodide on R/V *Roger Revelle*. R.M. measured iodate and assisted N.E. in measuring iodide on the R/V *Falkor*. J.W.M. designed and supervised the overall project as well as coordinating data synthesis from all cruises, supervising N.E., and integrating this water mass analysis with the principal project objectives. S.N. verified and revised the discussion of various physical oceanographic analyses, as well as guiding N.E. through methods for confirming her analysis of water mass and mesoscale eddies in the study region. A.R.B. directed sampling on the R/V *Falkor* as the Chief Scientist. A.H.D. was responsible for collecting, processing, and analyzing CTD, oxygen, nitrite, and phosphate data on RR1804. All authors offered feedback and revisions to this manuscript.

actually lead to a contraction in ODZs (Fu et al. 2018). This contradiction reveals that the interplay between ocean physics and the boundaries of ODZs requires more insight.

ODZs contain different ecosystems on microbial (Kalvelage et al. 2011, 2015; Ulloa et al. 2012; Carolan et al. 2015; Bianchi et al. 2018) and macroorganism scales (Deutsch et al. 2015; Chu and Gale 2017) from surrounding oxygenated waters. These ODZs contribute approximately 22–26 Tg of yearly fixed nitrogen loss from the ODZ in the Eastern Tropical North Pacific ocean (Gruber and Sarmiento 1997; Codispoti et al. 2001; Brandes and Devol 2002; specifically Gruber 2004), release approximately 6 Tg of the potent greenhouse gas nitrous oxide (Bianchi et al. 2012), and could act as a source of iron to the iron-limited Southern Ocean (Scholz et al. 2014).

ODZs occur due to a combination of nutrient-rich upwelling, sluggish mixing, and high biological surface productivity that positions them in the subtropics north and south of the equator (Stramma et al. 2010), called the Eastern Tropical North and South Pacific (ETNP and ETSP), appropriately. Both regions have a poleward undercurrent, known as the California Undercurrent (CUC) and Peru-Chile Undercurrent (PCUC), near the continental shelf, which are known to spawn mesoscale eddies that propagate west through their ODZs (Johnson and McTaggart 2010; Meinvielle and Johnson 2013; Nam et al. 2015). Mesoscale eddies increase productivity in both the ETNP and ETSP by transporting nutrients (Gruber et al. 2011), and coherent poleward undercurrent eddies possess elevated respiration rates compared to surrounding waters (Frenger et al. 2018) that lead to increased N_2O production (Arévalo-Martínez et al. 2016) and fixed nitrogen loss (Altabet et al. 2012).

The large-scale circulation responsible for the location of the ETNP ODZ within the Pacific Ocean, such as low ventilation (Kessler 2006; Stramma et al. 2010), and drivers for potential deoxygenation such as elevated respiration compounded on lower oxygen solubility at elevated temperature (Brewer and Peltzer 2016; Schmidtko et al. 2017) have been characterized. Nevertheless, thorough investigations into the water masses responsible for the depth range and vertical fine structure of the oxygen deficient layer have not been carried out. A water mass analysis deconvolutes an oceanographic transect into source water masses, allowing for specific features in the transect to be related to physical properties, and this water mass analysis focuses on the intermediate water masses that interact with the ODZ within this region. A water mass analysis of the ETSP, including the ODZ, was published based on the US GEOTRACES GP16 Eastern Pacific Zonal Transect (Peters et al. 2018), and this study provides a similar analysis of the ETNP ODZ. Previous works on the ODZs in the ETNP and ETSP have noted that their dissolved oxygen minima accompany the salinity maximum at isopycnals between 26.0 and 27.0 kg m^{-3}. That salinity maximum was identified as Equatorial Subsurface Water (ESSW), and this report aims to investigate the fidelity of the ODZ to this water mass, though we argue that the ESSW should be called the 13°C water (13CW) in the results and discussion.

In this article, ODZs are defined as regions where oxygen is absent or negligible and nitrate is the primary terminal electron acceptor (Devol 2015). There are three large, persistent ODZs in the ETNP off the coast of Mexico, the ETSP off Peru, and the Arabian Sea (Codispoti et al. 2001). In these regions, oxygen is at nanomolar concentrations and effectively zero under some conditions (Thamdrup et al. 2012), and there is a characteristic enrichment of nitrite associated with denitrification. Since the true dissolved oxygen concentrations are below the detection limit for conventional conductivity, temperature, and depth (CTD)-integrated SeaBird Electronics (SBE) 43 oxygen sensors (Revsbech et al. 2009), this nitrite enrichment is often used to define the depth where microbial nitrogen cycle processes are active.

Iodine is also an important redox active element in ODZ regimes. Iodate and iodide are the primary chemical species of inorganic iodine in the ocean, and the concentration of iodate dominates that of iodide within the oxygenated ocean (Luther et al. 1995). Within ODZs, iodate is reduced to iodide (Farrenkopf et al. 1997; Farrenkopf and Luther 2002), probably through microbial respiration. It has also been theorized that microbes can oxidize nitrite via iodate when oxygen is scarce (Babbin et al. 2017). Benthic inputs from continental margins also act as an iodide source (Zhou et al. 2018*b*). Iodide does not precipitate or scavenge easily, enabling it to accumulate in the water column. Once iodide accumulates, its oxidation to iodate cannot occur without oxygen so it is essentially conservative within the ODZ. This oxidation cannot occur because the reduction potential of iodate is less thermodynamically favorable than that of oxygen but more thermodynamically favorable than that of nitrate (Cutter et al. 2018), as depicted in Fig. 1, which enables the iodide and iodate proxies to be effective under both anoxia and hypoxia.

This intermediate reduction potential enables iodate to act as an indicator of deoxygenated water (Rue et al. 1997; Farrenkopf and Luther 2002; Cutter et al. 2018) and iodide as a proxy for shelf inputs (Zhou et al. 2018*b*). Due to the lower

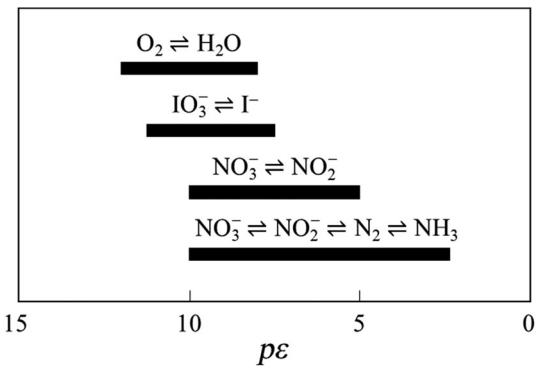

Fig. 1. Predicted oxidation/reduction ranges for relevant chemical species in seawater at pH 7.5 and practical salinity of 35. Data from Stumm and Morgan (1995) but presented in the style of Rue et al. (1997). Each redox couple has a range based on variations in activities within seawater.

rates of iodine redox interconversion (Tsunogai 1971; Bluhm et al. 2010) compared to rapid nitrite interconversion (Babbin et al. 2017), dissolved inorganic iodine species could serve as better indicators of the history of dissolved oxygen concentrations within a parcel of water.

Compounds such as nitrite, iodide, and iodate can be implemented to analyze the redox chemistry of deoxygenated waters. The spatial distributions of these compounds are compared to intermediate water masses deconvoluted from data generated in two longitudinal cruises in the ETNP ODZ. These comparisons are used to validate the results of the water mass analysis, in additional to cross-comparing the results between two independent cruises. With this information, this article explores the role of water masses in defining the oxygen deficient layer and the influence of hydrographic features on the secondary nitrite maximum.

Data and methods

Data collection and processing

This article focuses on data acquired by the R/V *Falkor* (FK180624) from June to July 2018, though includes data from the R/V *Roger Revelle* (RR1804) from March to April 2018 to test if results observed from the R/V *Falkor* are consistent between cruises and times (Fig. 2). These cruise transects will be referred to hereafter by their cruise names. Data from FK180624 and RR1804 are available at Rolling Deck 2 Repository (http://www.rvdata.us/catalog/FK180624) and (https://www.rvdata.us/search/cruise/RR1804). On both cruises, pressure, temperature, salinity, and oxygen data were acquired with a SBE 9/11 plus CTD, and the data collected during only upcasts were used to improve the quality of the data by limiting hysteresis in oxygen measurements via SBE 43 sensors. Nitrite and phosphate were measured onboard with the standard photometric methods (Strickland et al. 1972; Babbin et al. 2014), using a high-sensitivity 10 cm quartz cell (Starna) on FK180624, and iodate and iodide were measured via spectrometry and voltammetry, respectively (Moriyasu et al. 2020).

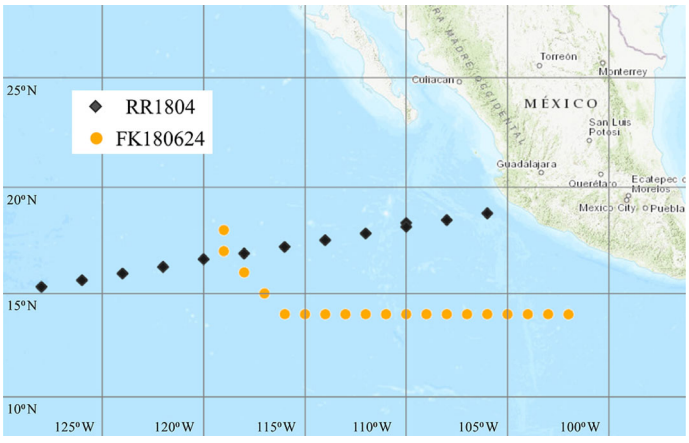

Fig. 2. Map detailing the cruise transects on the R/V *Falkor* (FK180624, orange circles) and the R/V *Roger Revelle* (RR1804, black diamonds). The FK180624 transect began at (14°N, 102°W) and ended at (18°N, 119°W), whereas the RR1804 transect began at (18.5°N, 110°W) and ended at (16°N, 124°W).

Methods

The primary result of this article is a water mass analysis produced via optimum multiparameter analysis (OMPA). The package for the OMPA was developed by Johannes Karstensen and Matthias Tomczak. This package operated in the MATLAB statistical computing language and the authors used MATLAB R2018b (The MathWorks, Inc. 2018). A previous version of this package can be found at https://omp.geomar.de/, though this version was not compatible with MATLAB R2018b and an updated version was distributed by Johannes Karstensen via personal communication. While this package relied on the EOS-80 seawater library rather than the current standard of TEOS-10 (http://www.teos-10.org/software.htm) (McDougall and Barker 2011), we used it to maintain continuity with previous water mass analyses. Instead, the authors adapted the OMPA package to input hydrographic data from TEOS-10 with IBM ILOG CPLEX Optimization Studio V12.8.0 as optimizer. For all the cruises, *in situ* temperature and salinity were converted to conservative temperature (Θ) and absolute salinity (S_A) with TEOS-10, and this information was used to calculate potential density referenced to surface (σ_θ) and spiciness (π). The modification of the OMPA package to input TEOS-10 maintains the continuity of the package while including updated oceanographic standards. Interpolated figures were generated using the contour and contour functions with linear interpolation in MATLAB and displayed contour lines were selected using scatter plots to ensure that the contours were representative of the distribution.

Due to the importance of mesoscale features on lateral transport, sea surface height anomaly (SSHA) data were retrieved from satellite altimetry. These data enabled us to analyze the influence of mesoscale eddies in shaping the water mass and nitrite distributions. The publicly accessible Copernicus Marine Environmental Monitoring Service (http://marine.copernicus.eu/) data product "Global Ocean Gridded L4 Sea Surface Height and Derived Variables NRT" with product id "SEALEVEL_GLO_PHY_L4_nrt_OBSERVATIONS_008_046" were used to visualize SSHA at the start date (30 June 2018), mid-date (08 July 2018), and end date (14 July 2018) of the FK180624 transect as well as the start date (06 April 2018) and end date (10 April 2018) of the RR1804 transect.

Water mass analysis

OMPA theory and application

Water masses are bodies of water in physical space that share a common formation history and thus similar properties

(Tomczak 1999). OMPA assumes that measured and calculated transect properties such as temperature, salinity, oxygen, phosphate, and/or potential vorticity can be decomposed into a linear combination of source water mass properties via inverse modeling (Karstensen and Tomczak 1997; Leffanue and Tomczak 2004; Peters et al. 2018). Each water mass is assigned a water type, which is a theoretical point in *n*-parameter space defined as the source or centered within the cluster of properties of the observed water mass (Tomczak 1999). During an OMPA, the fraction of each water mass must be non-negative (Acharya and Panigrahi 2016). Though the extent that water mass properties are conservative across a transect varies (Zhou et al. 2018*a*), classical OMPA has been used and described in a number of other oceanographic studies (Tomczak and Large 1989; Karstensen and Tomczak 1997; Poole and Tomczak 1999; Kim et al. 2010; Zhang et al. 2012; Acharya and Panigrahi 2016). Nevertheless, chemical parameters such as oxygen, phosphate, and nitrate are often only semi-conservative across large distances due to biological metabolisms. An extended version of OMPA was developed to account for nutrient nonconservative deviations from source water mass properties using the Redfield ratio combined with an internal parameter, the extent of remineralization (Poole and Tomczak 1999; Acharya and Panigrahi 2016; Peters et al. 2018), and this extended OMPA was implemented throughout this article.

Conservative temperature, absolute salinity, oxygen, phosphate, and spiciness were used for this OMPA study due to the availability and well-characterized nature of these parameters. Oxygen and phosphate were implemented independently, rather than as PO, and corrected with a variable representing the extent of remineralization. Nitrate was not used because denitrification in the ODZ renders this parameter non-conservative. While phosphate should also be non-conservative, omitting this parameter and remineralization worsens the quality of the OMPA fit, as seen in Section S7 in Supporting Information. The fit quality does not decrease in the 13CW or North Equatorial Pacific Intermediate Water (NEPIW) regions, suggesting that the basis set and methods are appropriate for these low oxygen waters. Instead, the lower fit quality appears in the oxic Antarctic Intermediate Water (AAIW) region, where oxygen-phosphate remineralization would be expected. The system of equations, calculations, and normalization applied for this OMPA are presented in Section S7 in Supporting Information and discussed thoroughly in Poole and Tomczak (1999) as well as Tomczak and Large (1989). Though nitrate and silicate are not present in the system of equations used in this analysis like they are in Poole and Tomczak (1999), spiciness is.

While spiciness (π) has not been implemented in water mass analyses before, it is a conservative state variable orthogonal to potential density anomaly (Flament 2002; Nam et al. 2015) commonly used to differentiate warmer, saltier waters at similar isopycnals within the California Current System (Thomson and Krassovski 2010; Meinvielle and Johnson 2013; Bograd et al. 2015; Nam et al. 2015). High spiciness has been correlated with lower dissolved oxygen and pH within the higher portion of Pacific Equatorial Water in the California Current System (Nam et al. 2015), and we include π in this study to aid as a proxy for dissolved oxygen in low oxygen waters. Other physical parameters besides π such as potential density (σ_θ) (Jenkins et al. 2015) and potential vorticity (You et al. 2000) have been used or considered in differentiating water masses.

This OMPA was weighted using the default coefficients in the package, {Θ, S_A, O_2, PO_4^{3-}, π, mass} = {24, 24, 7, 2, 7, 24}, and spiciness was weighted equally to oxygen since it is implemented as a proxy for oxygen in waters including and below the thermocline. In this study, extended OMPA was applied to analyze data from FK180624 and RR1804 cruises independently. Using five parameters enabled four water masses to be deconvoluted at once, due to the remineralization term. To facilitate this dimensional reduction, this water mass analysis was split between different potential density horizons for separate iterations of OMPA: surface ($\sigma_\theta < 26.0\,\mathrm{kg\,m^{-3}}$), intermediate ($26.0\,\mathrm{kg\,m^{-3}} < \sigma_\theta < 27.0\,\mathrm{kg\,m^{-3}}$), and deep ($\sigma_\theta > 27.0\,\mathrm{kg\,m^{-3}}$). These cruises lacked sufficient deep casts to provide a rigorous OMPA in this potential density horizon. Water mass distributions are plotted against σ_θ rather than depth or pressure due to the inherent coherence observed along the isopycnal surfaces. The OMPA results from FK180624 and RR1804 are presented in the results and discussion.

Previous water mass definitions

The basis set for the water masses in this analysis was identified via literature on general hydrography and circulation in the tropical Pacific (Wyrtki and Kendall 1967; Fiedler and Talley 2006), off Mexico (Warsh et al. 1973; Cepeda-Morales et al. 2013; Portela et al. 2016), the ETNP (Garfield et al. 1983), and within the ETSP (Silva et al. 2009; Ryabenko 2011; Peters et al. 2018). This literature suggests that the relevant water masses are Tropical Surface Water (TSW), Equatorial Surface Water (ESW), Pacific Subarctic Upper Water (PSUW), 13°C Water (13CW), NEPIW, AAIW, and Upper Circumpolar Deep Water (UCDW). Water masses such as Subtropical Subsurface Water (StSsW), Pacific Equatorial Water, and Pacific Intermediate Water were deemed to have too general of properties to be relevant for this analysis. A brief discussion of naming conventions for 13CW vs. StSsW vs. ESSW is included in Section 4.1.

Surface waters include TSW, ESW, and PSUW (Wyrtki and Kendall 1967; Warsh et al. 1973; Ryabenko 2011; Cepeda-Morales et al. 2013). Since FK180624 and RR1804 focused on the ODZ, surface sampling was not emphasized and most of the surface data came from FK180624. The OMPA results also indicate that some intermediate water could be seen bleeding into surface waters. Intermediate waters in these transects

include 13CW and NEPIW (Fiedler and Talley 2006; Ryabenko 2011; Peters et al. 2018), in addition to the oxygen deficient layer. AAIW contributes slightly to this potential density range and is included to improve the quality of the OMPA fit, though the center of AAIW is within deeper layers. For the purposes of this OMPA, NEPIW could be expressed as a linear combination of 13CW and AAIW, rendering its presence debatable by OMPA (Tomczak 1999). Nevertheless, previous studies have identified a Pacific Intermediate Water (Cepeda-Morales et al. 2013) and even Equatorial Pacific Intermediate Water (EqPIW) itself (Peters et al. 2018), justifying its inclusion. While ESW also appears to be a linear combination based on the Θ-S_A, relationship in Fig. 3a, it is an end-member in O_2-PO_4^{3-} space, as Fig. 3b depicts, and therefore must be a separate water mass.

The basis set of water types for this analysis was developed using previously established definitions for each water mass then refined using histograms of water properties from each transect. These definitions needed refining because previous literature on these water masses often defined them as a region on a *T-S* diagram that was too broad for this OMPA. Relative maxima in a Θ-S_A diagram indicated the Θ and S_A water type all water masses except PSUW and UCDW. Subsequent histograms of Θ vs. other parameters identified their water types. Using histograms to identify water masses has been established previously (Bourke and Pattullo 1974) and generates the precision necessary for this analysis. This treatment also implicitly includes any slight modifications that may have occurred over the lifetime of the water mass, but provide a more precise, robust local definition. The transformations that these water masses undergo are not well known, with the exception of AAIW, since the path of the 13CW has only been modeled (Qu et al. 2009), and the general pathway of the EqPIW has only been documented once before (Bostock et al. 2010). By defining these water masses locally, the uncertainties in water mass processing during transit can be removed.

The impact of location definitions can be seen most in the PSUW water mass. Since the California Current injects PSUW into the ETNP, it influences the region but does not have a large volume of water associated with it. Therefore, PSUW was defined as the coldest, freshest point on the Θ-S_A diagram. This assumption implies that the "true" PSUW value cannot be identified from this data, but waters that deviate from the TSW-13CW mixing line with lower temperatures and salinities have mixed with PSUW. Since this PSUW proxy is noticeably cooler and fresher (lower π) than native ETNP waters (Cepeda-Morales et al. 2013; Bograd et al. 2015; Nam et al. 2015), this assumption is reasonable.

The sources of the water masses in this transect are relatively well known. TSW is locally produced, whereas ESW originates from a mixture of upwelling and the Equatorial Undercurrent (EUC) (Wyrtki 1966; Tsuchiya et al. 1989). PSUW is transported equatorward to the ETNP from the colder North Pacific by the California Current (Lynn and Simpson 1990; Nam et al. 2015). 13CW is formed in the Tasman Sea (Tsuchiya 1981; Butler et al. 1992), but it is extensively modified in the South Pacific Subtropical Gyre before the EUC transports it to the Eastern Pacific (Qu et al. 2009). While the simulations in Qu et al. (2009) do not include 13CW in the northern hemisphere, it has been identified in this region due to transport by the Northern Subsurface Countercurrent (NSSCC) (Fiedler and Talley 2006). Pacific Intermediate Water has also been identified in this area (Cepeda-Morales et al. 2013) and based on its geographical location and physical properties, this water mass was specified as NEPIW rather than NPIW or EqPIW. Diapycnal mixing with Pacific Deep Water (PDW) and AAIW, with some influence from NPIW, forms NEPIW (Bostock et al. 2010). The AAIW forms in the Antarctic Circumpolar Current and has been well characterized (Talley 1996).

Basis set of water types

The combination of FK180624 and RR1804 data helped to create a robust basis set of water types (Tomczak 1999) for this OMPA, because the RR1804 data allowed the FK180624 basis set to be verified. Values for the basis set are presented in Table 1 and scatter plots of these water types are presented in Fig. 3. Conservative temperature and absolute salinity for surface water types varied between cruises, likely due to the changes in seasonal thermal stratification as FK180624 and RR1804 cruises were conducted in different seasons (spring

Table 1. Basis set of water types used in these water mass analyses.

Water mass	Θ/°C	S_A/g kg^{-1}	O_2/μmol kg^{-1}	PO_4^{3-}/μmol kg^{-1}	π
TSW	26.95 (FK); 26.56 (RR)	34.06 (FK); 33.83 (RR)	192.7	0.223	4.97 (FK); 4.36 (RR)
ESW	23.28 (FK); 21.26 (RR)	34.56 (FK); 34.44 (RR)	212.0	0.17	3.8 (FK); 3.3 (RR)
PSUW proxy	15.93 (FK); 16.71 (RR)	34.13	188.4	0.437	1.79 (FK); 1.91 (RR)
13CW	12.54 (FK); 13.08 (RR)	34.98 (FK); 34.95 (RR)	0.59 (FK); 0.69 (RR)	2.73	1.58 (FK); 1.68 (RR)
NEPIW	9.56	34.80	0.64 (FK); 0.90 (RR)	3.1	0.894
AAIW	6.03	34.70	4.8	3.48	0.418
UCDW proxy	1.42	34.87	118	2.67	−0.11

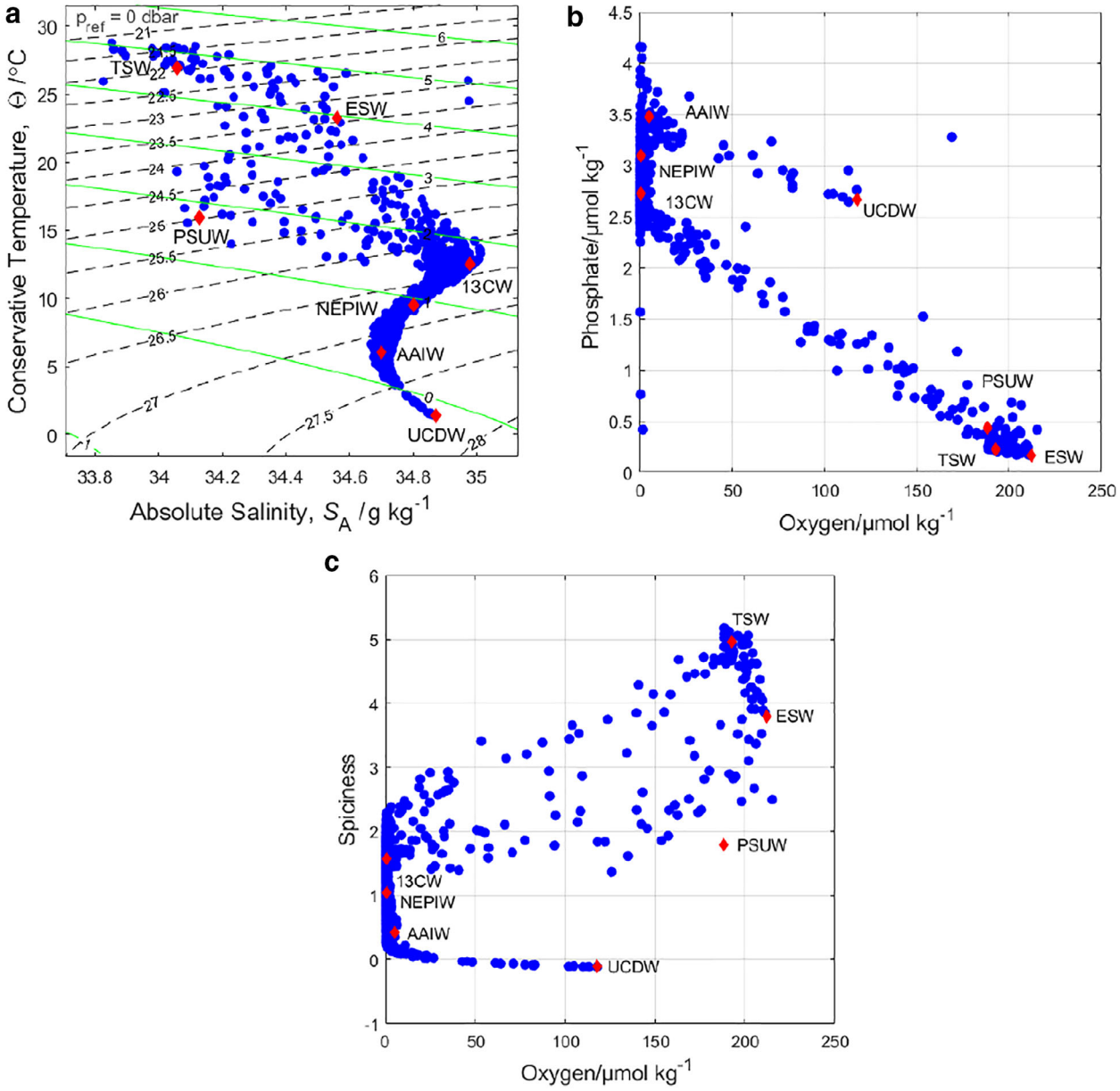

Fig. 3. Depiction of FK180624 basis set compared to sampled values from FK180624 and RR1804 data. (**a**) Conservative temperature vs. absolute salinity with isopycnal dashed lines in black and iso-π lines in green, (**b**) phosphate vs. oxygen where remineralization is not accounted for, and (**c**) spiciness vs. oxygen indicating that below the thermocline, higher spiciness correlates with lower dissolved oxygen.

and summer, respectively), and the FK180624 water types are preferred over the RR1804 types due to better vertical distribution of sampling. The presented values for dissolved oxygen in the 13CW and NEPIW water types are not necessarily the "true" dissolved oxygen for these water masses because the SBE 43 dissolved oxygen sensors cannot report quantitative concentrations within the range of dissolved oxygen concentrations in the ODZ. Nevertheless, these dissolved oxygen concentrations are consistent within each cruise, as depicted in Supporting Information Fig. S1.

Error analysis

The quality of OMPA fits was tested with the chi-squared goodness of fit test. A chi-squared parameter was calculated for each parameter of every data point, then summed to test the contribution of each parameter and the goodness of the OMPA fit itself. To account for autocorrelation, the degrees of freedom were reduced using the lag-1 correlation coefficient (Allen and Smith 1994; Hu et al. 2017). All fits presented have $p < 0.05$. Oxygen had the most error of any parameters, particularly when modeling the mixing of TSW and 13CW, likely

due to the large variance in oxygen concentrations between those two water masses.

Results and discussion

13CW shapes the ODZ

We label the salinity maximum (S_A = 34.8–35.0 g kg^{-1}) at 26.2σ_θ as 13CW following Tsuchiya (1981), though this water mass has been assigned other names such as the ESSW (Wyrtki and Kendall 1967) and the StSsW (Garfield et al. 1983). The water mass possessing this salinity maximum has been historically referred to as ESSW in the ETSP and southern hemisphere (Sobarzo et al. 2007; Silva et al. 2009; Peters et al. 2018), though 13CW has also been used (Johnson and McTaggart 2010). Off Mexico it is often referred to as StSsW (Warsh et al. 1973; Alvarez-Borrego and Schwartzlose 1979; Castro et al. 2000; Segovia-Zavala et al. 2010; Portela et al. 2016), though ESSW has also been used (Sañudo-Wilhelmy et al. 2012). This water mass has the lowest concentrations of dissolved oxygen and maximum spiciness of intermediate waters identified in this study.

A previous water mass analysis on the GEOTRACES GP16 transect included the ETSP ODZ and found that the ESSW, with a potential temperature around 13°C and a practical salinity around 34.9, dominated the low oxygen waters of the ODZ (Peters et al. 2018), similar to the ETNP ODZ. The ESSW, seen in the ETSP, and the low oxygen StSsW, seen in the ETNP, both branch off from the Equatorial Countercurrent (Fiedler and Talley 2006; Kessler 2006; Stramma et al. 2010). The NSSCC transports the ESSW to the ETNP from the equator, and the Southern Subsurface Countercurrent transports it to the ETSP (Stramma et al. 2010). The 13CW may originate from the Tasman Sea (Tsuchiya 1981), where the corresponding water properties are found during the summer (Butler et al. 1992), as formed via winter mixing with temperature-salinity properties and carried into the Eastern Pacific via the EUC. Models suggest that the South Pacific gyre extensively modifies the chemistry of the 13CW, and it can take up to 70 yr for it to be transported into the Eastern Equatorial Pacific (Qu et al. 2009). An eddy-resolving model of the ETNP ODZ determined that it is supplied primarily through its southern boundary around the 26.3 kg m^{-3} isopycnal. This model also suggested that most of the water entering the ETNP ODZ originates south of 30°S and has a mean transit time of 50 yr (Margolskee et al. 2019). These results support the 13CW as the primary water mass in the ETNP oxygen deficient layer and its origins in the Tasman Sea.

Since the 13CW and ESSW are both transported to the Eastern Pacific via the Equatorial Countercurrents/Undercurrents and share nearly equivalent temperature, salinity, and oxygen properties, these names are synonymous for the same water mass. Therefore, a single water mass, the 13CW, shapes both the ETNP and ETSP ODZs. This article refers to it as 13CW in an attempt to unify these three redundant location-specific names, since ESSW and StSsW refer to the same water mass (Wyrtki and Kendall 1967; Wijffels et al. 1996; Fiedler and Talley 2006). In addition, StSsW is often a broader definition that includes the 13CW mixed with other water masses. We chose to refer to this water mass as the 13CW since this water mass is not likely formed in the Equatorial Pacific, as the name ESSW implies. Unifying these water masses as the 13CW is important because this water mass is associated with diminished dissolved oxygen concentrations in the eastern Pacific Ocean.

The 13CW dominates both Pacific ODZs, and oxygen deficient conditions from the 13CW extend into NEPIW in the ETNP. In the ETSP, the 13CW is bounded by the EqPIW below (Peters et al. 2018), which is the same water mass as NEPIW but found closer to the equator and in the Southern hemisphere with a different nutrient profile (Bostock et al. 2010). In the ETSP, the EqPIW retains 20 μM O_2 (Peters et al. 2018), whereas our study identified dissolved oxygen concentrations below the limit of quantification for the SBE 43 oxygen sensors (Revsbech et al. 2009). Based on a depth profile of oxygen provided by an optode-based trace oxygen sensor, the NEPIW has 7–11 nM while this sensor could not detect oxygen within the 13CW (Larsen et al. 2016). The northerly decrease in oxygen from EqPIW to NEPIW is attributed to increased productivity north of the equator that depletes the oxygen of EqPIW (Bostock et al. 2010). EqPIW forms from subsurface mixing of AAIW, PDW, and some North Pacific Intermediate Water (Bostock et al. 2010), and this lack of ventilation leads to oxygen depletion, as does the lack of ventilation of 13CW.

The characteristic spiciness maximum of 13CW within the thermocline may factor into its role as the most deoxygenated water mass, since increases in spiciness lead to lower oxygen solubility and higher respiration rates as oxygen solubility decreases with increases in both temperature and salinity independently (Lynn and Simpson 1990; Brewer and Peltzer 2016). The salinity maximum of the 13CW reinforces the pycnocline that separates the intermediate layers from surface mixing, and this process maintains the redox gradient necessary to reach the ODZ conditions below (Fig. 8b). The relative depth of the 13°C isotherm, and by proxy the 13CW, is a significant driver for the volume of hypoxic waters in the Eastern Tropical Pacific because the shoaling of this water mass leads to enhanced productivity due to higher nutrient flux to the surface as well as increased respiration rates of the exported particles due to the higher temperatures (Deutsch et al. 2014). The long residence time and lack of ventilation of this water mass within the subtropical gyre or its transport under and parallel to the highly productive EUC could lead to biologically driven oxygen depletion as well. It is likely a combination of physical and biological factors that leads to the distinctive oxygen minima of 13CW in the ETNP (and ETSP) ODZ.

Offset between hydrographic results and secondary nitrite maximum

The intermediate waters contain the lowest oxygen concentrations in this region and their distributions can be seen in

Figs. 4, 5 for FK180624 and RR1804, respectively. The ODZ itself is defined as the space where oxygen concentrations are so low that nitrate competes and replaces it as the major oxidant. This shift in metabolism is associated with the secondary nitrite maximum, where nitrite accumulates as an intermediate in denitrification. The secondary nitrite maximum is often used to define the depth where microbial nitrogen cycle processes are active. This water mass analysis enables the transect to be deconvoluted into specific water masses, and we were interested in determining the relationship between the oxygen deficient layer and the 13CW. This relationship was analyzed by superimposing nitrite concentrations over the distribution of the 13CW. All OMPA fits were performed with 13CW, NEPIW, and AAIW. SSHA is present above each figure for ease of comparison and discussed further in the following section. Nevertheless, it is important to note that the SSHA values are daily averages while the CTD sampling occurred as quickly as every 5 h. This difference in sampling resolution renders quantitative analysis challenging. Also, SSHA integrates subsurface features and thus is not selective for intermediate features only in the potential density range of interest.

Elevated nitrite concentrations align well with greater than 70% 13CW, 110°W (Figs. 4, 5). East of 110°W, this nitrite feature extends below the isopycnal of 26.5σ_θ and into NEPIW (Fig. 4). This expansion of nitrite into deeper waters is attributed to increased productivity and particle fluxes closer to shore. The NEPIW water mass appears to interweave with the 13CW and nitrite does not accumulate within the NEPIW, though it has extremely low oxygen concentrations. The secondary nitrite maximum only fades where NEPIW uplifts into isopycnals of 26.2–26.4 kg m^{-3}, except at 106°W (Fig. 4). When FK180624 was sampling, 106°W is near the core of an anticyclonic eddy (Fig. 6), and strong downwelling of oxygenated waters (Supporting Information Fig. S5) interferes with the accumulation of nitrite. Nitrite accumulation also ends near the core of an anticyclonic eddy in Supporting Information Figs. S4, S5a.

Figure 5c depicts AAIW increasing west of 125°W around $\sigma\theta$ of 26.05 kg m^{-3} but the colocated maximum of the χ^2

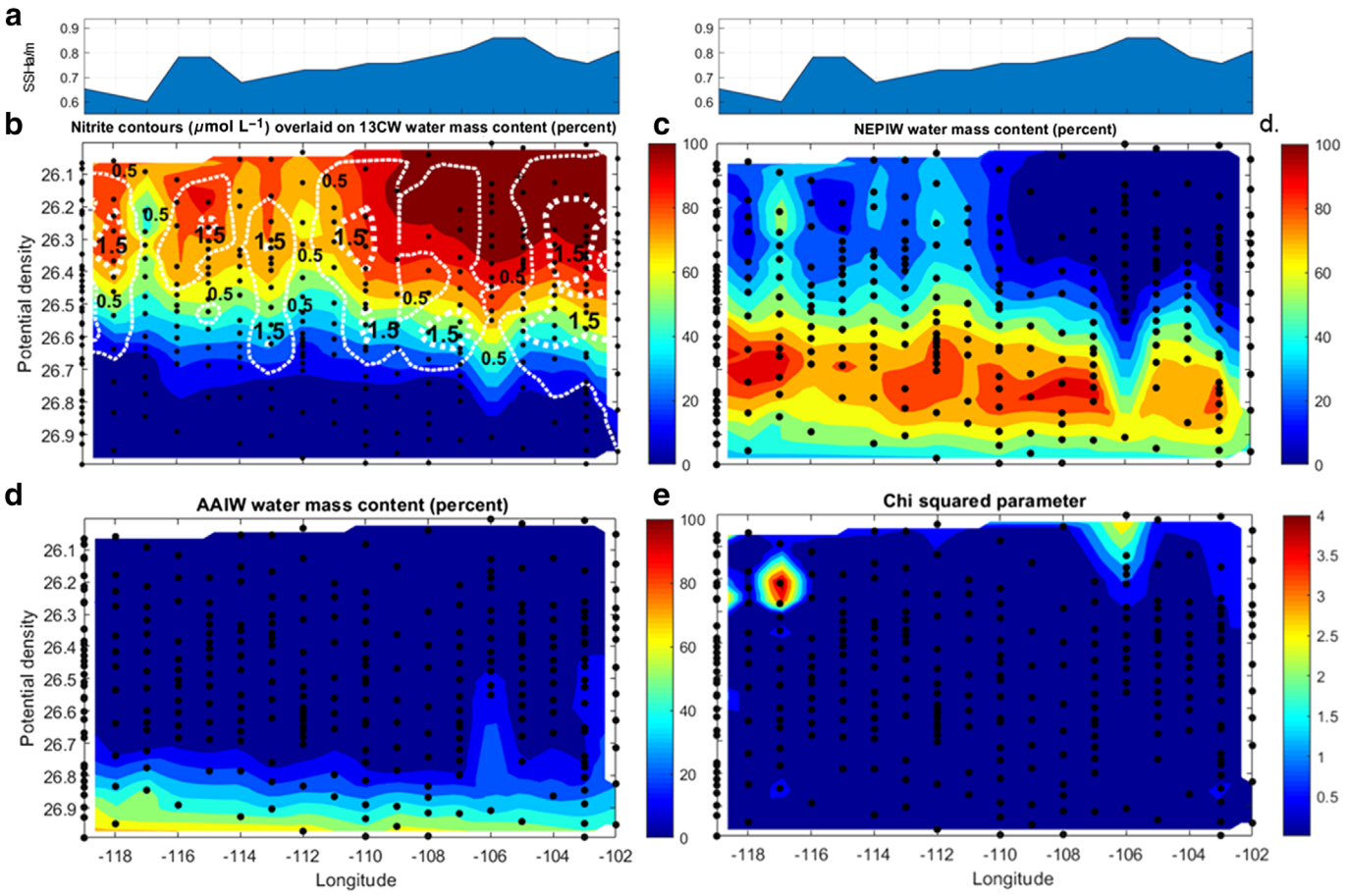

Fig. 4. (**a**) Daily averaged SSHA above geoid in meters for each station. Percentages of (**b**) 13CW, (**c**) NEPIW, (**d**) AAIW, and (**e**) error (χ^2 parameter) for the FK180624 intermediate waters with $p < 0.05$. The percent 13CW water mass figure includes white contours of nitrite concentration at 0.5 and 1.5 μM, allowing a comparison between the 13CW water mass and the secondary nitrite maximum. Black dots represent sampling locations.

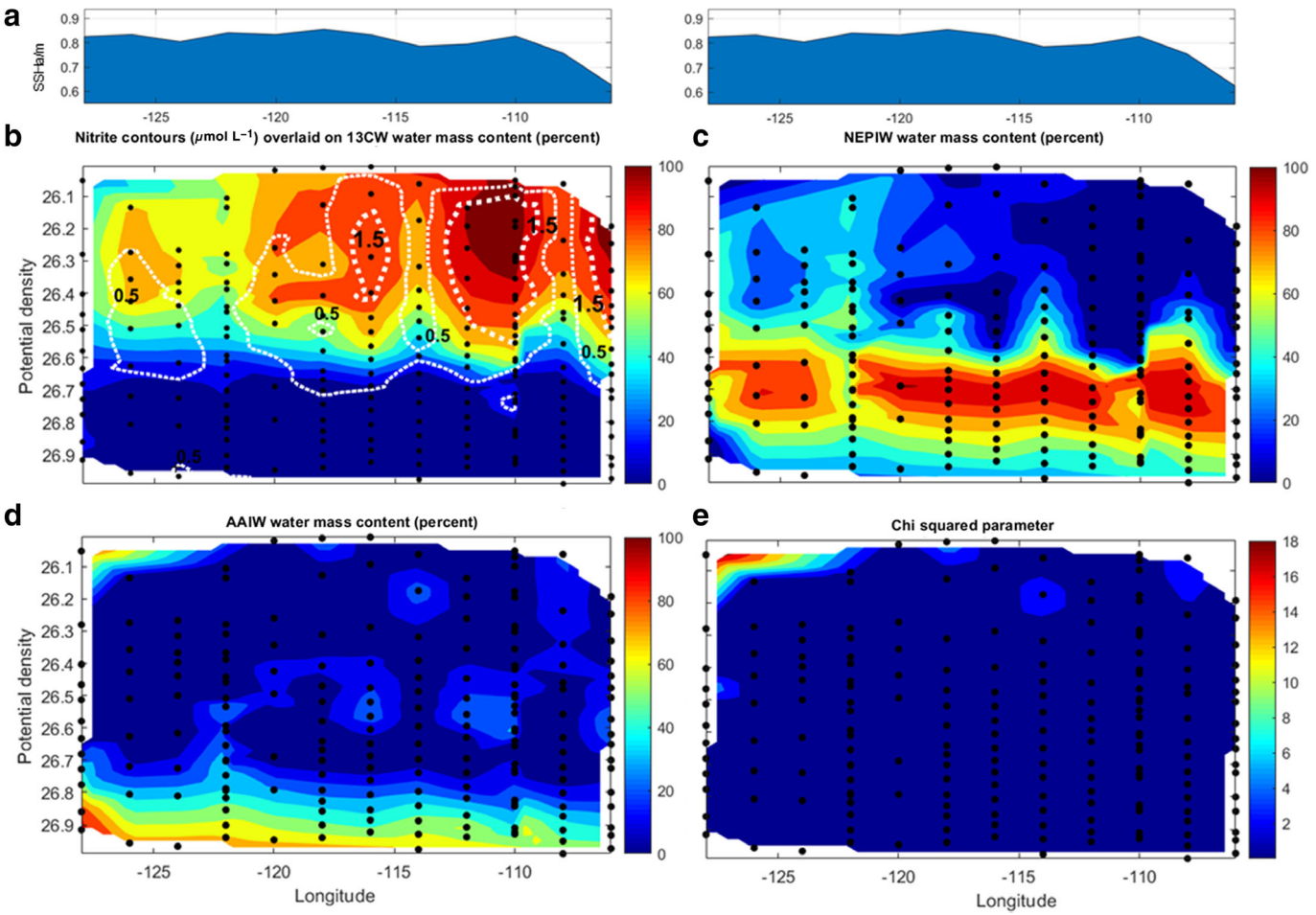

Fig. 5. Same as Fig. 4 but for the RR1804 with $p < 0.05$.

parameter in Fig. 5d indicates that the OMPA had significant error in fitting this region. AAIW is not expected at this shallow isopycnal, so it is likely the water mass observed in this point is PSUW-proxy. PSUW is far fresher than 13CW and NEPIW, but PSUW-proxy was not included as a water type within the intermediate OMPA. The freshest water mass in the intermediate OMPA is AAIW, hence why it was selected by the optimization algorithm, but Fig. 5d indicates that this attribution is incorrect.

Role of mesoscale eddies on 13CW distribution and nitrite accumulation

The secondary nitrite maximum centered at isopycnals of 26.3–26.4 kg m^{-3} does not align with a water mass; rather, the CUC has been identified at this potential density range (Meinvielle and Johnson 2013; Nam et al. 2015). Mesoscale features created by the CUC maintain this isopycnal while propagating west. SSHA is a common tool for identifying mesoscale dynamics (Chelton et al. 2011; Nan et al. 2011; Nam et al. 2012), and can even identify subsurface eddy dynamics (Chaigneau et al. 2011; Pegliasco et al. 2015). Analysis of satellite altimetry reveals that minima in SSHA accompany a shift from 13CW to NEPIW at isopycnals of 26.2–26.4 kg m^{-3}, observed specifically at 117°W and 114°W in FK180624 and 120°W and 114°W in RR1804.

Subsurface mesoscale eddies are responsible for the maxima in SSHA observed in Figs. 6 and 7. These mesoscale eddies transport 13CW westward, extending the range of the ODZ and the volume where nitrite accumulates. Subsurface mesoscale eddies caused by poleward undercurrents possess elevated respiration rates compared to surrounding waters (Frenger et al. 2018) that lead to increased N_2O production (Arévalo-Martínez et al. 2016) and fixed nitrogen loss (Altabet et al. 2012). The shift in the core of the 13CW to deeper isopycnals in the western region of these transects, particularly noticeable in Fig. 5, is due to the propagation of mesoscale eddies at the 26.3–26.4 kg m^{-3} isopycnals of the CUC, which are deeper than the 26.1–26.3 kg m^{-3} isopycnals of the core of the 13CW. Figure 8b reveals the 13CW dominates up to isopycnal 25.8 kg m^{-3} as well. The mesoscale eddies observed on FK180624 appear to be transient (Supporting Information Fig. S5), but coherent subsurface eddies can be formed via poleward undercurrents (Frenger et al. 2018).

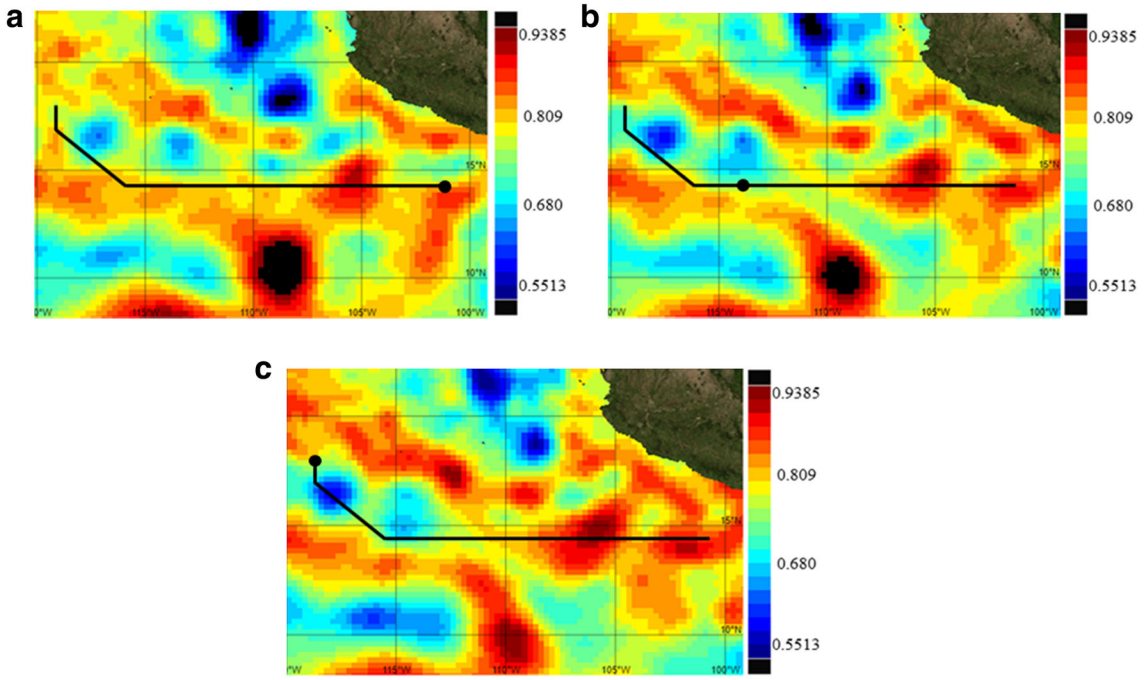

Fig. 6. Sea surface height anomaly above geoid at (**a**) 30 June 2018, (**b**) 08 July 2018, and (**c**) 14 July 2018. The maximum value shown in red is 0.939 m, whereas the minimum value shown in blue color is 0.551 m for all maps. The black dot represents the approximate location of the R/V *Falkor* during the transect, traveling westward, while the mesoscale features including the eddies propagate westward.

Coupling between the nitrogen and iodine cycles in low oxygen waters

In addition to nitrite, iodine redox chemistry can also be an indicator for deoxygenated water (Fig. 1). While the appearance of iodide would be expected as an indicator for the absence of oxygen, lateral advection of iodide from reducing shelf sediments complicates this analysis (Moriyasu et al. 2019; Cutter et al. 2018; Zhou et al. 2018*a*). The distribution of iodide within the oxygen deficient layer is depicted in Fig. 8a. A station from a previous cruise demonstrates that the 13CW shoals onto the continental shelf (Section S6 in Supporting Information), so this water mass contains the highest iodide concentrations from this additional source and its inherent low oxygen concentration. Since oxygen is required for iodide to convert into iodate (Luther et al. 1995), the turnover of iodide is slower than nitrite and influenced primarily by mixing processes, and these factors cause a more patchy distribution of iodide than nitrite (Moriyasu et al. 2019).

The absence of iodate is a better indicator for low oxygen conditions than elevated iodide because of iodide's additional benthic source. Iodate deficiency indicates a history of deoxygenated conditions within a parcel of water. Figure 8b displays a general alignment of the nitrite and iodate proxies for the oxycline within the 13CW as sampled in FK180624, which exists in shallower waters with intermediate iodate concentrations and zero nitrite. These results demonstrate that the 13CW houses the redox gradient leading to the oxygen deficient layer, as seen in the decrease of iodate concentration with depth. This trend in iodate persists until NEPIW appears and the differing concentrations of iodate in these water masses exemplifies the increased oxygen in NEPIW compared

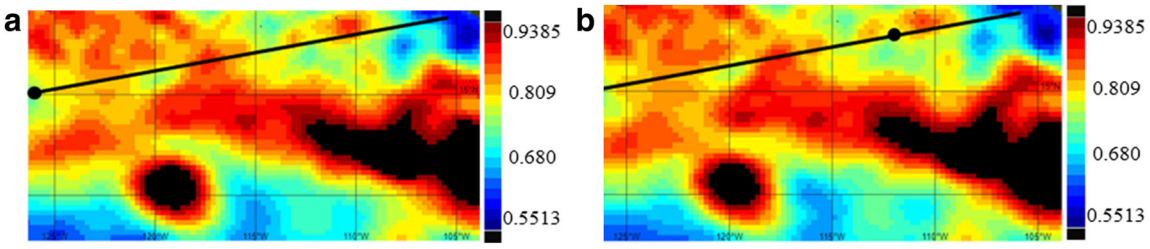

Fig. 7. Same as Fig. 6 but for the RR1804, where is sampled at (**a**) 06 April 2018 and (**b**) 10 April 2018. Note that RR1804 had several legs and its full cruise path is documented in Moriyasu et al. (2019).

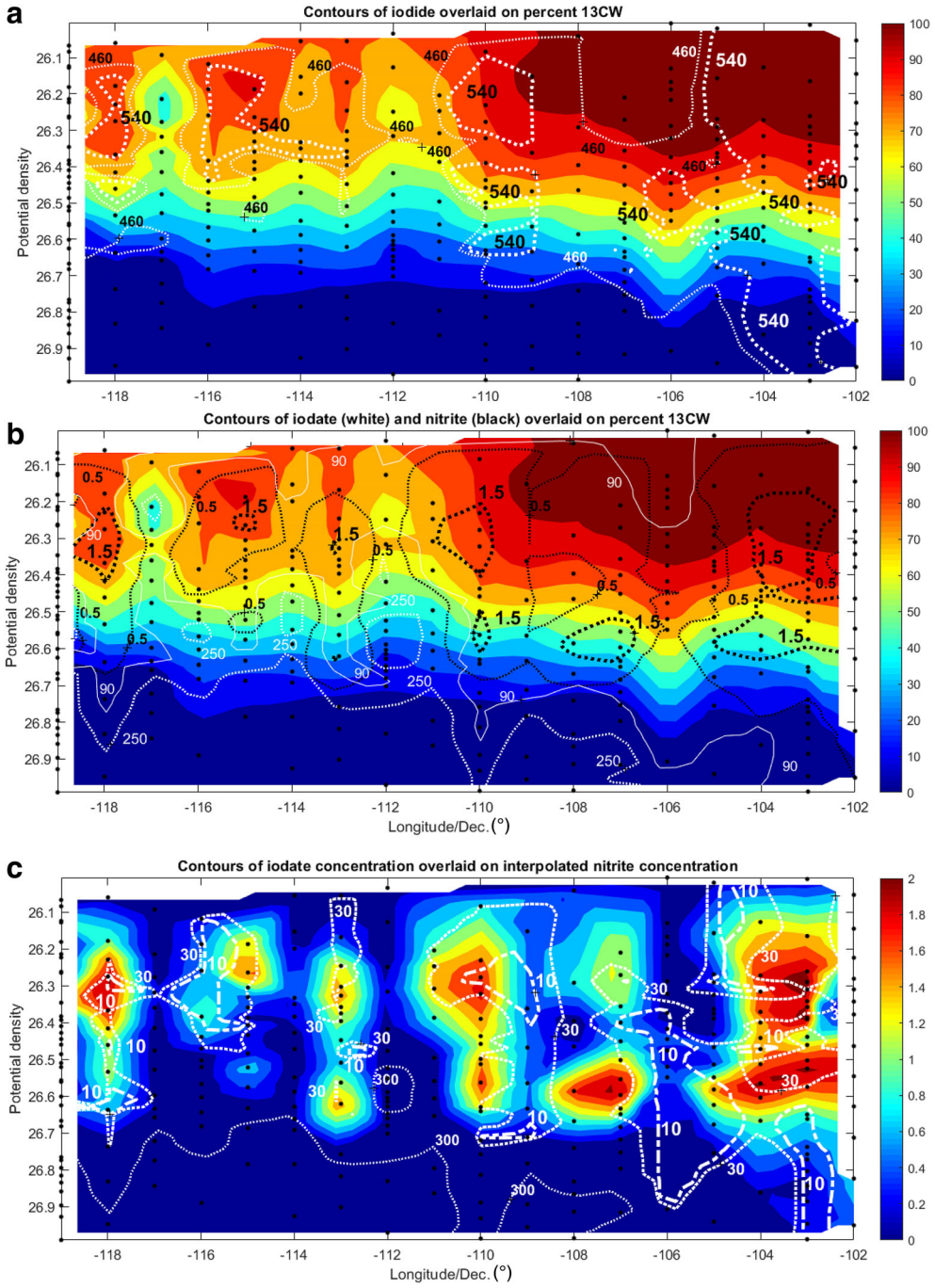

Fig. 8. Percent of 13CW with (**a**) white contours of 460 and 540 nM iodide and (**b**) with black contours of 0.5 and 1.5 μM nitrite and white contours of 90 and 250 nM iodate. (**c**) The concentration of nitrite in μM with white contours of 10, 30, and 300 nM iodate, appropriately. Black dots represent sampling locations on FK180624.

to 13CW. Broadly, the secondary nitrite maximum overlaps with minima in iodate, but regions with iodate minima, seen in Fig. 8c, appear to avoid maxima in nitrite. The accumulation of nitrite occurs below the iodate gradient within the 13CW, which could suggest that nitrite accumulation may be hindered by the presence of iodate.

Within the ETNP ODZ, there are water parcels with zero iodate (Moriyasu et al. 2019), unlike in the ETSP ODZ (Cutter et al. 2018). Figure 8c demonstrates that these parcels exist around and between the secondary nitrite maxima in the ETNP ODZ, since these nitrite maxima are shaped by subsurface mesoscale eddies. In the ETSP ODZ, the 13CW and

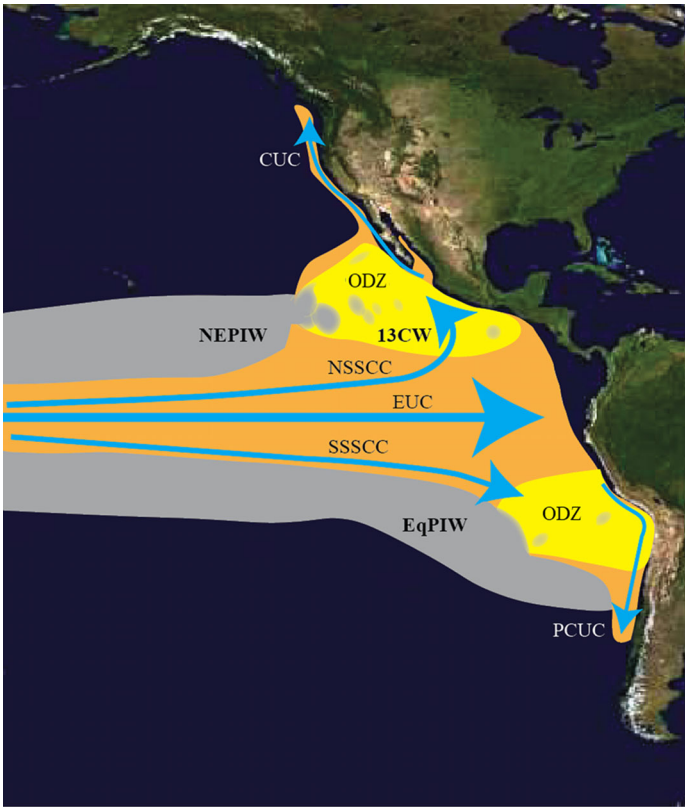

Fig. 9. The above schematic depicts the extent of 13CW (orange) and NEPIW/EqPIW (gray) across the Eastern Pacific at isopycnals of 26.2–26.5 kg m^{-3} as well as the currents that transport 13CW (blue) based on this work and cited literature. When the 13CW overlaps with a shadow circulation region, an ODZ forms (yellow), until NEPIW/EqPIW upwells and replaces the 13CW. Pockets of NEPIW appear within the ETNP as the mesoscale eddies carrying 13CW wean.

corresponding secondary nitrite maximum is a coherent region, as seen in Section S5 in Supporting Information. The ETSP does not appear to require subsurface mesoscale features for nitrite accumulation, whereas the periodic accumulation of nitrite and the 13CW in the ETNP reveals that subsurface mesoscale features are necessary for the secondary nitrite maximum (Supporting Information Fig. S5). Nevertheless, the denitrification observed in the ETSP may be relic features from coastal waters (Sonnerup et al. 2019), and subsurface eddies may be one of the vehicle for transporting this denitrified water. Complete iodate reduction also appears to be a property of the ETNP.

We cannot currently explain the complete iodate reduction in the ETNP compared to the ETSP due to the number of differences between these systems. There is stronger upwelling in the ETSP than the ETNP (Pennington et al. 2006), which could supply more iodate from EqPIW to the ETSP ODZ than the iodate supply of NEPIW to the ETNP ODZ. The ETSP is also thinner and more dynamic than the ETNP, which could allow other waters to mix into the 13CW in the ETSP. There are also differences in primary productivity. If high nitrite concentrations correlate with high denitrification rates and thus high denitrifier iodate utilization rates, where iodate is used as a terminal electron acceptor, it would be surprising that locations with high nitrite concentrations do not align with locations where iodate is absent. Nevertheless, it is possible that the water parcels where iodate is absent have been embedded within the ODZ and isolated from oxygen longer, while the parcels with high nitrite have been recently exposed to materials at the continental margin. These margin inputs boost denitrification or entrain nitrite from the shelf, even though these water parcels may not have been embedded within the ODZ as long. This discussion remains hypothetical until more is learned about iodate utilization rates and mechanisms as concentrations approach zero.

Brief ETSP water mass comparison

When the ETSP water mass analysis (Peters et al. 2018) is repeated for 26.0–27.5 kg m^{-3}, as discussed in the Supporting Information, the 13CW and the secondary nitrite maximum are coupled as seen in the ETNP. EqPIW appears to replace the 13CW past 100°W, and the secondary nitrite maximum disappears along with the 13CW. In the ETSP data presented, the signature of mesoscale eddies cannot be seen from satellite altimetry (Supporting Information Fig. S6e), though previous studies have identified infrequent subsurface eddies from the PCUC (Johnson and McTaggart 2010). From these observations, subsurface mesoscale eddies are likely infrequent in the ETSP, and nitrite could accumulate independently of them. Contrary to these observations, denitrification in the ETSP has been suggested to be a relic signal from coastal processes (Sonnerup et al. 2019), and eddies could be a potential explanation for this analysis. In the ETNP, nitrite only accumulates within subsurface mesoscale eddies, suggesting that the elevated respiration rate of these features may be required for nitrite accumulation in the ETNP. Nevertheless, the presence of the 13CW vs. NEPIW/EqPIW shapes the secondary nitrite maximum in both Pacific ODZs and influences seasonal hypoxia off South America (Sobarzo et al. 2007; Silva et al. 2009).

Conclusion

The overlap between a single water mass, the 13CW, and physiochemical forcings that drive deoxygenation creates the environment required for denitrification within the secondary nitrite maximum in the ETNP ODZ. The 13CW is centered at approximately 150 dbars and isopycnals of 26.2–26.3 kg m^{-3} and it is thickest on the eastern side of the transects. SBE 43 oxygen sensors report the lowest dissolved oxygen concentrations in this water mass for both FK180624 and RR1804, ranging from 0.6 to 0.7 μM. While these concentrations are below the linear response range for these sensors (Revsbech et al. 2009), the maximum spiciness of 13CW suggest that it has the minimum oxygen of any water mass. This inference is

supported by the lack of detection of oxygen by trace oxygen sensors with a detection limit of 5 nM (Larsen et al. 2016).

The deeper low oxygen water mass, the NEPIW centered around 400 dbars and isopycnals of 26.7–26.8 kg m^{-3}, also has an oxygen concentration below the detection limit of conventional SBE43 sensors, but not as low as the 13CW. This conclusion can be inferred by the distribution of nitrite vs. the distribution of 13CW (Figs. 4a, 5a), because nitrite does not accumulate within the NEPIW. An eddy-resolving model of the ETNP ODZ also identified a primary oxygen source centered around the 26.8 kg m^{-3} isopycnal through its northwestern boundary (Margolskee et al. 2019), which matches the potential density range of NEPIW within this region, its trajectory through the eastern Pacific (Bostock et al. 2010), and the nitrite and iodate measured in the ETNP as redox indicators. Larsen et al. (2016) also measured 7–11 nM oxygen in the ETNP at a transition slightly shallower than 400 m.

Despite the 13CW having the lowest oxygen concentrations in the water column, the region where nitrite accumulates does not align with its core. Also, the relative water mass content (%) of 13CW does not decrease monotonically across these transects because subsurface mesoscale eddies intersperse Northern Equatorial Pacific Intermediate Water (NEPIW) into the isopycnals of 13CW. At the western edge of the transect, it appears that NEPIW completely eclipses 13CW, but there are insufficient data to support this claim definitively. Within latitudinal and longitudinal ranges of the ODZ as controlled by the physiochemical drivers of deoxygenation, the vertical fine structure of the ETNP ODZ is shaped by subsurface mesoscale eddies and their influence on the ratio of 13CW to NEPIW.

A separate OMPA in the California Current System using locally defined water types has deconvolved upper and lower Pacific Equatorial Waters (PEW) at isopycnals of 26.2 and 26.8 kg m^{-3} (Bograd et al. 2018) responsible for deoxygenation within the Southern California Bight (Bograd et al. 2008, 2015; Nam et al. 2015). These definitions fit 13CW and NEPIW almost exactly and the entrainment of 13CW within mesoscale eddies in the ETNP suggests that this water mass is present in the CUC. These results suggest that the 13CW water mass influences diminished oxygen concentrations across the entire Eastern Pacific Ocean from subtropical gyres poleward to Alaska and Chile. Figure 9 depicts the known distribution of 13CW, the currents that transport it, and role of NEPIW/EqPIW in defining the boundaries of the 13CW and ODZs.

Climate change drives present and future ocean deoxygenation (Helly and Levin 2004; Stramma et al. 2010; Gilly et al. 2013; Gallo and Levin 2016; Breitburg et al. 2018; Fu et al. 2018; Levin 2018). Current global biogeochemical models struggle with modeling oxygen due to the complex set of factors that control its distribution (Fu et al. 2018). Since the 13CW and NEPIW are the primary low oxygen waters in the eastern Pacific, other tracers for these water masses could be implemented to simulate oxygen concentrations and the advection of these low oxygen waters.

Iodine speciation clearly differentiates the 13CW and the NEPIW in the ETNP ODZ. Within the 13CW, iodate ranges from 0 to 200 nM, compared to its 200–400 nM concentration range within the NEPIW. Iodide reaches 400–850 nM concentrations within the 13CW since this water mass shoals onto the shelf. The shoaling of the 13CW onto the continental shelf (Section S6 in Supporting Information) suggests that the 13CW may act as a conduit in the shelf-to-basin shuttle for reduced species from shelf sediments to the deep interior of the ETNP. This phenomenon may be the first steps in the shelf-to-basin iron shuttle (Severmann et al. 2008; Scholz et al. 2014), which transfers iron and other reducing compounds like iodide off the continental shelf and into ocean basins. In the case of iron, oxidation of the reduced intermediate water iron plume leads to its precipitation onto the continental slope (Heller et al. 2017). Within this 13CW conduit, mesoscale features resulting from the CUC drive parcels of water enriched by sediment pore waters. The continental shelf appears to have significantly more influence on the 13CW than the NEPIW, resulting in notable difference in both iodide and iodate for these two water masses.

Compared to the iodide maxima around 13CW, iodide is oxidized within NEPIW such that there is 200–300 nM iodate, compared to the 0–40 nM iodate concentrations in the 13CW. This difference in iodine speciation supports the higher dissolved oxygen concentration of NEPIW compared to 13CW, because the larger iodate concentrations in the NEPIW suggest that it is a more oxidizing water mass. The iodate concentration gradient is a sensitive indicator for dissolved oxygen concentrations between isopycnals of 25.8 and 26.2 kg m^{-3}. Since the 25.8–26.2 kg m^{-3} isopycnals also contain the transition into the 13CW water mass, the 13CW plays an important role in setting the oxycline required for deeper ODZ conditions between isopycnals of 26.2 and 26.6 kg m^{-3}. In addition, if iodate and nitrite are metabolically coupled, then the iodate concentration gradient may also influence the depth horizon at which nitrite begins to accumulate.

This distribution of iodate, iodide, denitrification, and oxygen between these two waters influences the conditions of the California Current System, since the CUC transports both water masses with a summer shift towards 13CW (Nam et al. 2015). A water mass-based distribution may be seen in other redox active compounds besides iodine. For example, 13CW appears to possess fourfold higher concentrations of riboflavin than NEPIW (Sañudo-Wilhelmy et al. 2012). Identifying these water masses as sources of PEW enables a better understanding of the nutrient fluxes within the California Current System, an economically important region. It is interesting to note that within the ETNP ODZ, iodate is depleted, whereas this phenomenon does not occur in the ETSP or Arabian Sea ODZ (Farrenkopf and Luther 2002; Cutter et al. 2018), though the Arabian Sea does not share water masses with the Pacific ODZs (You and Tomczak 1993; Acharya and Panigrahi 2016). Iodate depletion occurs outside of eddy-induced secondary nitrite

maxima (Fig. 8c), and future research on iodate reaction mechanisms is required to understand this observation fully.

Within the California Current System, the 13CW is seasonally transported and associated with lower dissolved oxygen and pH than the NEPIW, which are both locally referred to as PEW (Nam et al. 2015). While iodine was not measured in Nam et al. (2015), the seasonal advection of 13CW is likely correlated with a shift from iodate to iodide-rich waters which could be used as a tracer for the relative contributions of these two water masses. Silva et al. (2009) suggested that integrated inorganic nitrogen deficit, calculated as N^* (Gruber and Sarmiento 1997), could be used as a tracer for the 13CW as it is advected from the ODZ regions. The gradient in iodate concentration entering the 13CW core in the ETNP indicates that dissolved inorganic iodine species may be more accurate, since denitrification is likely not consistent across this redox gradient. Focusing on the 13CW signature would improve attempts at modeling deoxygenation in the Pacific Ocean due to the strong correlation of this water mass with low dissolved oxygen and high spiciness. Rather than using fundamental models to predict ODZ expansion in the future, simulating the accumulation of 13CW could result in more precise estimates. Estimating the fluxes and shoaling of the 13CW could also be implemented to anticipate advection-driven coastal deoxygenation.

Identifying the role of the 13CW, NEPIW, and subsurface mesoscale eddies on the ETNP ODZ allows some climate change predictions to be made. As climate change increases surface ocean temperatures, water stratification will increase and isopycnals will deepen, decreasing dissolved oxygen concentrations (Xiu et al. 2018). These conditions will lead to the surface-13CW redoxcline stretching as the core of the 13CW deepens due to stratification but upper waters decrease in dissolved oxygen concentration. A more interesting consequence is the elevation of the CUC isopycnal with temperature (Meinvielle and Johnson 2013). The extent of this undercurrent's variability with temperature has not been characterized but likely leads to the seasonal advection of 13CW vs. NEPIW. Eddies from the CUC lead to nitrite accumulation in the ETNP ODZ, and increased temperatures could better align the 13CW and the secondary nitrite maximum. The amount of 13CW in the ETNP and ETSP may also increase, as the EUC accelerates (Coats and Karnauskas 2018), though the net accumulation can only occur if the Tsuchiya jets and poleward undercurrents remain at a constant or lower velocity.

References

Acharya, S. S., and M. K. Panigrahi. 2016. Eastward shift and maintenance of Arabian Sea oxygen minimum zone: Understanding the paradox. Deep-Sea Res. Part I Oceanogr. Res. Pap. **115**: 240–252. doi:10.1016/j.dsr.2016.07.004

Allen, M. R., and L. A. Smith. 1994. Investigating the origins and significance of low-frequency modes of climate variability. Geophys. Res. Lett. **21**: 883–886. doi:10.1029/94GL00978

Altabet, M. A., E. Ryabenko, L. Stramma, D. W. R. Wallace, M. Frank, P. Grasse, and G. Lavik. 2012. An eddy-stimulated hotspot for fixed nitrogen-loss from the Peru oxygen minimum zone. Biogeosciences **9**: 4897–4908. doi:10.5194/bg-9-4897-2012

Alvarez-Borrego, S., and R. A. Schwartzlose. 1979. Water masses of the Gulf of California. Cienc. Mar. **6**: 43–63. doi:10.7773/cm.v6i1.350

Arévalo-Martínez, D. L., A. Kock, C. R. Löscher, R. A. Schmitz, L. Stramma, and H. W. Bange. 2016. Influence of mesoscale eddies on the distribution of nitrous oxide in the Eastern Tropical South Pacific. Biogeosciences **13**: 1105–1118. doi:10.5194/bg-13-1105-2016

Babbin, A. R., R. G. Keil, A. H. Devol, and B. B. Ward. 2014. Organic matter stoichiometry, flux, and oxygen control nitrogen loss in the ocean. Science **344**: 406–408. doi:10.1126/science.1248364

Babbin, A. R., B. D. Peters, C. W. Mordy, B. Widner, K. L. Casciotti, and B. B. Ward. 2017. Multiple metabolisms constrain the anaerobic nitrite budget in the Eastern Tropical South Pacific: Nitrogen dynamics in the Eastern Tropical South Pacific. Global Biogeochem. Cycles. **13**: 1–14. doi:10.1002/2016GB005407

Bianchi, D., J. P. Dunne, J. L. Sarmiento, and E. D. Galbraith. 2012. Data-based estimates of suboxia, denitrification, and N_2O production in the ocean and their sensitivities to dissolved O_2. Global Biogeochem. Cycles **26**: 1–13. doi:10.1029/2011GB004209

Bianchi, D., T. S. Weber, R. Kiko, and C. Deutsch. 2018. Global niche of marine anaerobic metabolisms expanded by particle microenvironments. Nat. Geosci. **11**: 263–268. doi:10.1038/s41561-018-0081-0

Bluhm, K., P. Croot, K. Wuttig, and K. Lochte. 2010. Transformation of iodate to iodide in marine phytoplankton driven by cell senescence. Aquat. Biol. **11**: 1–15. doi:10.3354/ab00284

Bograd, S., I. Schroeder, and M. Jacox. 2018. A water mass history of the Southern California current system. Geophys. Res. Lett. **46**: 6690–6698. doi:10.1029/2019GL082685

Bograd, S. J., C. G. Castro, E. D. Lorenzo, D. M. Palacios, H. Bailey, W. Gilly, and F. P. Chavez. 2008. Oxygen declines and the shoaling of the hypoxic boundary in the California Current. Geophys. Res. Lett. **35**: 1–6. doi:10.1029/2008GL034185

Bograd, S. J., and others. 2015. Changes in source waters to the Southern California Bight. Deep-Sea Res. Part II Top. Stud. Oceanogr. **112**: 42–52. doi:10.1016/j.dsr2.2014.04.009

Bostock, H. C., B. N. Opdyke, and M. J. M. Williams. 2010. Characterising the intermediate depth waters of the Pacific Ocean using $\delta^{13}C$ and other geochemical tracers. Deep-Sea Res. Part I Oceanogr. Res. Pap. **57**: 847–859. doi:10.1016/j.dsr.2010.04.005

Bourke, R. H., and J. G. Pattullo. 1974. Seasonal variation of the water mass along the Oregon-northern California coast. Limnol. Oceanogr. **19**: 190–198. doi:10.4319/lo.1974.19.2.0190

Brandes, J. A., and A. H. Devol. 2002. A global marine-fixed nitrogen isotopic budget: Implications for Holocene nitrogen cycling. Global Biogeochem. Cycles **16**: 67-1–67-14. doi:10.1029/2001GB001856

Breitburg, D., et al. 2018. Declining oxygen in the global ocean and coastal waters. Science **359**: 1–11. doi:10.1126/science.aam7240

Brewer, P. G., and E. T. Peltzer. 2016. Ocean chemistry, ocean warming, and emerging hypoxia: Commentary. J. Geophys. Res. Oceans **121**: 3659–3667. doi:10.1002/2016JC011651

Butler, E. C. V., J. A. Butt, E. J. Lindstrom, P. C. Teldesley, S. Pickmere, and W. F. Vincent. 1992. Oceanography of the subtropical convergence zone around southern New Zealand. N. Z. J. Mar. Freshw. Res. **26**: 131–154. doi:10.1080/00288330.1992.9516509

Carolan, M. T., J. M. Smith, and J. M. Beman. 2015. Transcriptomic evidence for microbial sulfur cycling in the eastern tropical North Pacific oxygen minimum zone. Front. Microbiol. **6**: 1–8. doi:10.3389/fmicb.2015.00334

Castro, R., A. S. Mascarenhas, R. Durazo, and C. A. Collins. 2000. Seasonal variation of the temperature and salinity at the entrance to the Gulf of California, Mexico. Cienc. Mar. **26**: 561–583. doi:10.7773/cm.v26i4.621

Cepeda-Morales, J., G. Gaxiola-Castro, E. Beier, and V. M. Godínez. 2013. The mechanisms involved in defining the northern boundary of the shallow oxygen minimum zone in the eastern tropical Pacific Ocean off Mexico. Deep-Sea Res. Part I Oceanogr. Res. Pap. **76**: 1–12. doi:10.1016/j.dsr.2013.02.004

Chaigneau, A., M. Le Texier, G. Eldin, C. Grados, and O. Pizarro. 2011. Vertical structure of mesoscale eddies in the eastern South Pacific Ocean: A composite analysis from altimetry and Argo profiling floats. J. Geophys. Res. Oceans **116**: 1–16. doi:10.1029/2011JC007134

Chelton, D. B., M. G. Schlax, and R. M. Samelson. 2011. Global observations of nonlinear mesoscale eddies. Prog. Oceanogr. **91**: 167–216. doi:10.1016/j.pocean.2011.01.002

Chu, J. W. F., and K. S. P. Gale. 2017. Ecophysiological limits to aerobic metabolism in hypoxia determine epibenthic distributions and energy sequestration in the northeast Pacific ocean. Limnol. Oceanogr. **62**: 59–74. doi:10.1002/lno.10370

Coats, S., and K. B. Karnauskas. 2018. A role for the equatorial undercurrent in the ocean dynamical thermostat. J. Clim. **31**: 6245–6261. doi:10.1175/JCLI-D-17-0513.1

Codispoti, L. A., J. A. Brandes, J. P. Christensen, A. H. Devol, S. W. A. Naqvi, H. W. Paerl, and T. Yoshinari. 2001. The oceanic fixed nitrogen and nitrous oxide budgets: Moving targets as we enter the anthropocene? Sci. Mar. **65**: 85–105. doi:10.3989/scimar.2001.65s285

Cutter, G. A., J. W. Moffett, M. C. Nielsdóttir, and V. Sanial. 2018. Multiple oxidation state trace elements in suboxic waters off Peru: In situ redox processes and advective/diffusive horizontal transport. Mar. Chem. **201**: 77–89. doi:10.1016/j.marchem.2018.01.003

Deutsch, C., and others. 2014. Centennial changes in North Pacific anoxia linked to tropical trade winds. Science **345**: 665–668. doi:10.1126/science.1252332

Deutsch, C., A. Ferrel, B. Seibel, H.-O. Portner, and R. B. Huey. 2015. Climate change tightens a metabolic constraint on marine habitats. Science **348**: 1132–1135. doi:10.1126/science.aaa1605

Devol, A. H. 2015. Denitrification, anammox, and N_2 production in marine sediments. Ann. Rev. Mar. Sci. **7**: 403–423. doi:10.1146/annurev-marine-010213-135040

Diaz, R. J., and R. Rosenberg. 2008. Spreading dead zones and consequences for marine ecosystems. Science **321**: 926–929. doi:10.1126/science.1156401

Farrenkopf, A. M., G. W. Luther, V. W. Truesdale, and C. H. Van Der Weijden. 1997. Sub-surface iodide maxima: Evidence for biologically catalyzed redox cycling in Arabian Sea OMZ during the SW intermonsoon. Deep-Sea Res. Part II Top. Stud. Oceanogr. **44**: 1391–1409. doi:10.1016/S0967-0645(97)00013-1

Farrenkopf, A. M., and G. W. Luther. 2002. Iodine chemistry reflects productivity and denitrification in the Arabian Sea: Evidence for flux of dissolved species from sediments of western India into the OMZ. Deep-Sea Res. Part II Top. Stud. Oceanogr. **49**: 2303–2318. doi:10.1016/S0967-0645(02)00038-3

Fiedler, P. C., and L. D. Talley. 2006. Hydrography of the eastern tropical Pacific: A review. Prog. Oceanogr. **69**: 143–180. doi:10.1016/j.pocean.2006.03.008

Flament, P. 2002. A state variable for characterizing water masses and their diffusive stability: Spiciness. Prog. Oceanogr. **54**: 493–501. doi:10.1016/S0079-6611(02)00065-4

Frenger, I., D. Bianchi, C. Stührenberg, A. Oschlies, J. Dunne, C. Deutsch, E. Galbraith, and F. Schütte. 2018. Biogeochemical role of subsurface coherent eddies in the ocean: Tracer cannonballs, hypoxic storms, and microbial stewpots? Global Biogeochem. Cycles **32**: 226–249. doi:10.1002/2017GB005743

Fu, W., F. Primeau, J. Keith Moore, K. Lindsay, and J. T. Randerson. 2018. Reversal of increasing tropical ocean hypoxia trends with sustained climate warming. Global Biogeochem. Cycles **32**: 551–564. doi:10.1002/2017GB005788

Gallo, N. D., and L. A. Levin. 2016. Fish ecology and evolution in the world's oxygen minimum zones and implications of ocean deoxygenation. Adv. Mar. Biol. **74**: 117–198. doi:978-0-12-803607-5

Garfield, P. C., T. T. Packard, G. E. Friederich, and L. A. Codispoti. 1983. A subsurface particle maximum layer and enhanced microbial activity in the secondary nitrite

maximum of the northeastern tropical Pacific Ocean. J. Mar. Res. **41**: 747–768. doi:10.1357/002224083788520496

Gilly, W. F., J. M. Beman, S. Y. Litvin, and B. H. Robison. 2013. Oceanographic and biological effects of shoaling of the oxygen minimum zone. Ann. Rev. Mar. Sci. **5**: 393–420. doi:10.1146/annurev-marine-120710-100849

Gruber, N. 2004. The dynamics of the marine nitrogen cycle and its influence on atmospheric CO_2 variations, p. 97–148. *In* M. Follows and T. Oguz [eds.], The ocean carbon cycle and climate. Springer. doi:978-1-4020-2086-5

Gruber, N., and J. L. Sarmiento. 1997. Global patterns of marine nitrogen fixation and denitrification. Global Biogeochem. Cycles **11**: 235–266. doi:10.1029/97GB00077

Gruber, N., Z. Lachkar, H. Frenzel, P. Marchesiello, M. Münnich, J. C. McWilliams, T. Nagai, and G.-K. Plattner. 2011. Eddy-induced reduction of biological production in eastern boundary upwelling systems. Nat. Geosci. **4**: 787–792. doi:10.1038/ngeo1273

Heller, M. I., P. J. Lam, J. W. Moffett, C. P. Till, J.-M. Lee, B. M. Toner, and M. A. Marcus. 2017. Accumulation of Fe oxyhydroxides in the Peruvian oxygen deficient zone implies non-oxygen dependent Fe oxidation. Geochim. Cosmochim. Acta **211**: 174–193. doi:10.1016/j.gca.2017.05.019

Helly, J. J., and L. A. Levin. 2004. Global distribution of naturally occurring marine hypoxia on continental margins. Deep-Sea Res. Part I Oceanogr. Res. Pap. **51**: 1159–1168. doi:10.1016/j.dsr.2004.03.009

Hu, J., J. Emile-Geay, and J. Partin. 2017. Correlation-based interpretations of paleoclimate data – where statistics meet past climates. Earth Planet. Sci. Lett. **459**: 362–371. doi:10.1016/j.epsl.2016.11.048

Jenkins, W. J., W. M. Smethie, E. A. Boyle, and G. A. Cutter. 2015. Water mass analysis for the U.S. GEOTRACES (GA03) North Atlantic sections. Deep-Sea Res. Part II Top. Stud. Oceanogr. **116**: 6–20. doi:10.1016/j.dsr2.2014.11.018

Johnson, G. C., and K. E. McTaggart. 2010. Equatorial Pacific 13°C water eddies in the eastern subtropical South Pacific Ocean. J. Phys. Oceanogr. **40**: 226–236. doi:10.1175/2009JPO4287.1

Kalvelage, T., and others. 2011. Oxygen sensitivity of anammox and coupled N-cycle processes in oxygen minimum zones. PLoS One **6**: e29299. doi:10.1371/journal.pone.0029299

Kalvelage, T., and others. 2015. Aerobic microbial respiration in oceanic oxygen minimum zones. PLoS One **10**: e0133526. doi:10.1371/journal.pone.0133526

Karstensen, J., and M. Tomczak. 1997. Ventilation processes and water mass ages in the thermocline of the southeast Indian Ocean. Geophys. Res. Lett. **24**: 2777–2780. doi:10.1029/97GL02708

Kessler, W. S. 2006. The circulation of the eastern tropical Pacific: A review. Prog. Oceanogr. **69**: 181–217. doi:10.1016/j.pocean.2006.03.009

Kim, I.-N., D.-H. Min, D. H. Kim, and T. Lee. 2010. Investigation of the physicochemical features and mixing of East/Japan Sea Intermediate Water: An isopycnic analysis approach. J. Mar. Res. **68**: 799–818. doi:10.1357/002224010796673849

Larsen, M., P. Lehner, S. M. Borisov, I. Klimant, J. P. Fischer, F. J. Stewart, D. E. Canfield, and R. N. Glud. 2016. In situ quantification of ultra-low O_2 concentrations in oxygen minimum zones: Application of novel optodes. Limnol. Oceanogr.: Methods **14**: 784–800. doi:10.1002/lom3.10126

Leffanue, H., and M. Tomczak. 2004. Using OMP analysis to observe temporal variability in water mass distribution. J. Mar. Syst. **48**: 3–14. doi:10.1016/j.jmarsys.2003.07.004

Levin, L. A. 2018. Manifestation, drivers, and emergence of open ocean deoxygenation. Ann. Rev. Mar. Sci. **10**: 229–260. doi:10.1146/annurev-marine-121916-063359

Luther, G. W., J. Wu, and J. B. Cullen. 1995. Redox chemistry of iodine in seawater, p. 135–155. *In* Aquatic chemistry. American Chemical Society. doi:978-0-8412-2921-1

Lynn, R. J., and J. J. Simpson. 1990. The flow of the undercurrent over the continental borderland off southern California. J. Geophys. Res. Oceans **95**: 12995–13008. doi:10.1029/JC095iC08p12995

Margolskee, A., H. Frenzel, S. Emerson, and C. Deutsch. 2019. Ventilation pathways for the North Pacific oxygen deficient zone. Global Biogeochem. Cycles **33**: 875–890. doi:10.1029/2018GB006149

McDougall, T. J., and P. M. Barker. 2011. Getting started with TEOS-10 and the Gibbs Seawater (GSW) oceanographic toolbox. SCOR/IAPSO WG127. doi:978-0-646-55621-5

Meinvielle, M., and G. C. Johnson. 2013. Decadal water-property trends in the California Undercurrent, with implications for ocean acidification. J. Geophys. Res. Oceans **118**: 6687–6703. doi:10.1002/2013JC009299

Moriyasu, R., N. Evans, K. Bolster, D. S. Hardisty, and J. W. Moffett. 2019. The distribution and redox speciation of iodine in the Eastern Tropical North Pacific Ocean. Global Biogeochem. Cycles. doi:10.1029/2019GB006302

Nam, S., D. Kim, and W. M. Moon. 2012. Observed impact of mesoscale circulation on oceanic response to Typhoon Man-Yi (2007). Ocean Dyn. **62**: 1–12. doi:10.1007/s10236-011-0490-8

Nam, S., Y. Takeshita, C. A. Frieder, T. Martz, and J. Ballard. 2015. Seasonal advection of Pacific Equatorial Water alters oxygen and pH in the Southern California Bight. J. Geophys. Res. Oceans **120**: 5387–5399. doi:10.1002/2015JC010859

Nan, F., Z. He, H. Zhou, and D. Wang. 2011. Three long-lived anticyclonic eddies in the northern South China Sea. J. Geophys. Res. Oceans **116**: 1–15. doi:10.1029/2010JC006790

Pegliasco, C., A. Chaigneau, and R. Morrow. 2015. Main eddy vertical structures observed in the four major Eastern Boundary Upwelling Systems. J. Geophys. Res. Oceans **120**: 6008–6033. doi:10.1002/2015JC010950

Pennington, J. T., K. L. Mahoney, V. S. Kuwahara, D. D. Kolber, R. Calienes, and F. P. Chavez. 2006. Primary production in the eastern tropical Pacific: A review. Prog. Oceanogr. **69**: 285–317. doi:10.1016/j.pocean.2006.03.012

Peters, B. D., W. J. Jenkins, J. H. Swift, C. R. German, J. W. Moffett, G. A. Cutter, M. A. Brzezinski, and K. L. Casciotti. 2018. Water mass analysis of the 2013 US GEOTRACES eastern Pacific zonal transect (GP16). Mar. Chem. **201**: 6–19. doi:10.1016/j.marchem.2017.09.007

Poole, R., and M. Tomczak. 1999. Optimum multiparameter analysis of the water mass structure in the Atlantic Ocean thermocline. Deep-Sea Res. Part I Oceanogr. Res. Pap. **46**: 1895–1921. doi:10.1016/S0967-0637(99)00025-4

Portela, E., and others. 2016. Water masses and circulation in the tropical Pacific off central Mexico and surrounding areas. J. Phys. Oceanogr. **46**: 3069–3081. doi:10.1175/JPO-D-16-0068.1

Qu, T., S. Gao, I. Fukumori, R. A. Fine, and E. J. Lindstrom. 2009. Origin and pathway of equatorial 13°C water in the Pacific identified by a simulated passive tracer and its adjoint. J. Phys. Oceanogr. **39**: 1836–1853. doi:10.1175/2009JPO4045.1

Revsbech, N. P., L. H. Larsen, J. Gundersen, T. Dalsgaard, O. Ulloa, and B. Thamdrup. 2009. Determination of ultra-low oxygen concentrations in oxygen minimum zones by the STOX sensor. Limnol. Oceanogr.: Methods **7**: 371–381. doi:10.4319/lom.2009.7.371

Rue, E. L., G. J. Smith, G. A. Cutter, and K. W. Bruland. 1997. The response of trace element redox couples to suboxic conditions in the water column. Deep-Sea Res. Part I Oceanogr. Res. Pap. **44**: 113–134. doi:10.1016/S0967-0637(96)00088-X

Ryabenko, E. 2011. Nitrogen isotopes in the atlantic and pacific oxygen minimum zones. Doctoral thesis. Christian-Albrechts Universität Kiel.

Sañudo-Wilhelmy, S. A., and others. 2012. Multiple B-vitamin depletion in large areas of the coastal ocean. Proc. Natl. Acad. Sci. USA **109**: 14041–14045. doi:10.1073/pnas.1208755109

Schmidtko, S., L. Stramma, and M. Visbeck. 2017. Decline in global oceanic oxygen content during the past five decades. Nature **542**: 335–339. doi:10.1038/nature21399

Scholz, F., S. Severmann, J. McManus, A. Noffke, U. Lomnitz, and C. Hensen. 2014. On the isotope composition of reactive iron in marine sediments: Redox shuttle versus early diagenesis. Chem. Geol. **389**: 48–59. doi:10.1016/j.chemgeo.2014.09.009

Segovia-Zavala, J. A., M. L. Lares, F. Delgadillo-Hinojosa, A. Tovar-Sánchez, and S. A. Sañudo-Wilhelmy. 2010. Dissolved iron distributions in the central region of the Gulf of California, México. Deep-Sea Res. Part I Oceanogr. Res. Pap. **57**: 53–64. doi:10.1016/j.dsr.2009.10.007

Severmann, S., T. W. Lyons, A. Anbar, J. McManus, and G. Gordon. 2008. Modern iron isotope perspective on the benthic iron shuttle and the redox evolution of ancient oceans. Geology **36**: 487–490. doi:10.1130/G24670A.1

Silva, N., N. Rojas, and A. Fedele. 2009. Water masses in the Humboldt Current System: Properties, distribution, and the nitrate deficit as a chemical water mass tracer for Equatorial Subsurface Water off Chile. Deep-Sea Res. Part II Top. Stud. Oceanogr. **56**: 1004–1020. doi:10.1016/j.dsr2.2008.12.013

Sobarzo, M., L. Bravo, D. Donoso, J. Garcés-Vargas, and W. Schneider. 2007. Coastal upwelling and seasonal cycles that influence the water column over the continental shelf off central Chile. Prog. Oceanogr. **75**: 363–382. doi:10.1016/j.pocean.2007.08.022

Sonnerup, R. E., B. X. Chang, M. J. Warner, and C. W. Mordy. 2019. Timescales of ventilation and consumption of oxygen and fixed nitrogen in the eastern tropical South Pacific oxygen deficient zone from transient tracers. Deep Sea Research Part I: Oceanographic Research Papers 103080. doi:10.1016/j.dsr.2019.103080

Stramma, L., G. C. Johnson, E. Firing, and S. Schmidtko. 2010. Eastern Pacific oxygen minimum zones: Supply paths and multidecadal changes. J. Geophys. Res. Oceans **115**: 1–12. doi:10.1029/2009JC005976

Strickland, J. D. H., T. R. Parsons, and J. D. H. Strickland. 1972. A practical handbook of seawater analysis. Fisheries Research Board of Canada. doi:10.1002/iroh.19700550118.

Stumm, W., and J. Morgan. 1995. Aquatic chemistry: Chemical equilibria and rates in natural waters, 3rd ed. Wiley. doi:978-0-471-51185-4

Talley, L. D. 1996. Antarctic intermediate water in the South Atlantic, p. 219–238. *In* The South Atlantic. Springer. doi:978-3-642-80353-6

Thamdrup, B., T. Dalsgaard, and N. P. Revsbech. 2012. Widespread functional anoxia in the oxygen minimum zone of the Eastern South Pacific. Deep-Sea Res. Part I Oceanogr. Res. Pap. **65**: 36–45. doi:10.1016/j.dsr.2012.03.001

The MathWorks, Inc. 2018. MATLAB release 2018b.

Thomson, R. E., and M. V. Krassovski. 2010. Poleward reach of the California Undercurrent extension. J. Geophys. Res. Oceans **115**: 1–9. doi:10.1029/2010JC006280

Tomczak, M. 1999. Some historical, theoretical and applied aspects of quantitative water mass analysis. J. Mar. Res. **57**: 275–303. doi:10.1357/002224099321618227

Tomczak, M., and D. G. B. Large. 1989. Optimum multiparameter analysis of mixing in the thermocline of the eastern Indian Ocean. J. Geophys. Res. Oceans **94**: 16141–16149. doi:10.1029/JC094iC11p16141

Tsuchiya, M. 1981. The origin of equatorial ^{13}C water. J. Phys. Oceanogr. **11**: 794–812. doi:0022-3670/81/060794-19

Tsuchiya, M., R. Lukas, R. A. Fine, E. Firing, and E. Lindstrom. 1989. Source waters of the Pacific Equatorial Undercurrent. Prog. Oceanogr. **23**: 101–147. doi:10.1016/0079-6611(89)90012-8

Tsunogai, S. 1971. Iodine in the deep water of the ocean. Deep-Sea Res. Oceanogr. Abstr. **18**: 913–919. doi:10.1016/0011-7471(71)90065-9

Ulloa, O., D. E. Canfield, E. F. DeLong, R. M. Letelier, and F. J. Stewart. 2012. Microbial oceanography of anoxic oxygen minimum zones. Proc. Natl. Acad. Sci. USA **109**: 15996–16003. doi:10.1073/pnas.1205009109

Warsh, C. E., K. L. Warsh, and R. C. Staley. 1973. Nutrients and water masses at the mouth of the Gulf of California. Deep-Sea Res. Oceanogr. Abstr. **20**: 561–570. doi:10.1016/0011-7471(73)90080-6

Wijffels, S. E., J. M. Toole, H. L. Bryden, R. A. Fine, W. J. Jenkins, and J. L. Bullister. 1996. The water masses and circulation at 10°N in the Pacific. Deep-Sea Res. Part I Oceanogr. Res. Pap. **43**: 501–544. doi:10.1016/0967-0637(96)00006-4

Wyrtki, K. 1966. Oceanography of the Eastern Equatorial Pacific Ocean. Oceanogr. Mar. Biol. Ann. Rev. **4**: 33–68.

Wyrtki, K., and R. Kendall. 1967. Transports of the Pacific equatorial countercurrent. J. Geophys. Res. **72**: 2073–2076. doi:10.1029/JZ072i008p02073

Xiu, P., F. Chai, E. N. Curchitser, and F. S. Castruccio. 2018. Future changes in coastal upwelling ecosystems with global warming: The case of the California Current System. Scientific Reports **8**: 2866. doi:10.1038/s41598-018-21247-7

You, Y., and M. Tomczak. 1993. Thermocline circulation and ventilation in the Indian Ocean derived from water mass analysis. Deep-Sea Res. Part I Oceanogr. Res. Pap. **40**: 13–56. doi:10.1016/0967-0637(93)90052-5

You, Y., N. Suginohara, M. Fukasawa, I. Yasuda, I. Kaneko, H. Yoritaka, and M. Kawamiya. 2000. Roles of the Okhotsk Sea and Gulf of Alaska in forming the North Pacific Intermediate Water. J. Geophys. Res. Oceans **105**: 3253–3280. doi:10.1029/1999JC900304

Zhang, L., J. Zhang, P. W. Swarzenski, and Z. Liu. 2012. Radium isotope tracers to evaluate coastal ocean mixing and residence times, p. 331–343. M. Baskaran (ed.) *In* Handbook of environmental isotope geochemistry. Springer-Verlag Berlin Heidelberg. doi:10.1007/978-3-642-10637-8_17.

Zhou, P., X. Song, Y. Yuan, X. Cao, W. Wang, L. Chi, and Z. Yu. 2018*a*. Water mass analysis of the East China Sea and interannual variation of Kuroshio subsurface water intrusion through an optimum multiparameter method. J. Geophys. Res. Oceans **123**: 3723–3738. doi:10.1029/2018JC013882

Zhou, P., X. Song, Y. Yuan, W. Wang, L. Chi, X. Cao, and Z. Yu. 2018*b*. Intrusion of the Kuroshio Subsurface Water in the southern East China Sea and its variation in 2014 and 2015 traced by dissolved inorganic iodine species. Prog. Oceanogr. **165**: 287–298. doi:10.1016/j.pocean.2018.06.011

Acknowledgments

We would like to express our appreciation for the various assistance received when working on this project. The captain and crew of the FK180624 enabled the collection of the high-resolution data required for the precise water mass analysis. Onboard FK180624, Dalton Hardisty assisted in measuring iodide. The publicly available OMPA script written by Johannes Karstensen and Matthias Tomczak at https://omp.geomar.de/ enabled N.E. to implement this water mass analysis, in addition to feedback from Brian Peters, the author of the 2018 Eastern Pacific Zonal Transect water mass analysis. Peters also provided his basis set of water types from the ETSP for comparison. Daniele Bianchi provided useful clarification on the classification of mesoscale features observed in these transects. Seth John and Julien Emile-Geay provided MATLAB scripts for interpolation and lag-1 correction for autocorrelation, respectively. Naomi Levine provided a suggestion to ease figure readability. Kareesa Kron provided useful criticism and suggestions on statistical analysis for this article. We would like to thank two anonymous reviewers for comments that helped us clarify this work. This study has been conducted using E.U. Copernicus Marine Service Information. Data from FK180624 and RR1804 are available at Rolling Deck 2 Repository (http://www.rvdata.us/). A Schmidt Ocean Institute grant to Karen Casciotti and A.R.B. supported the FK180624 cruise. Additional support was provided by the MIT Ally of Nature Award and by the generous support of Dr. Bruce L. Heflinger to A.R.B. NSF OCE-1636332 and NSF DEB-1542240 supported the RR1804 cruise and the University of Southern California supported N.E. and R.M. on the FK180624 cruise. NSF OCE-1657958 also provided support.

Conflict of Interest

None declared.

Submitted 12 June 2019
Revised 07 November 2019
Accepted 23 December 2019

Associate editor: Lauren Juranek